Thin Solid Films, 206 (1991) 294–299

Two-channel spectroscopic polarization modulation ellipsometry: A new technique for the analysis of thin SiO_2 films

G. E. Jellison, Jr.

Solid State Division, Oak Ridge National Laboratory, Oak Ridge, TN 37831-6056 (U.S.A.)

Abstract

A new spectroscopic ellipsometer is described, where the incoming light is dynamically polarized using a photoelastic modulator, and the reflected light is separated into orthogonally polarized beams using a Wollaston prism. Both beams are detected using photomultiplier tubes whose bias voltage is dynamically controlled for constant d.c. All three of the associated ellipsometry parameters ($N = \cos 2\psi$, $S = \sin 2\psi \sin \Delta$, $C = \sin 2\psi \cos \Delta$) can be determined simultaneously in a single scan (240–840 nm or 5.16–1.47 eV).

This instrument was used to study the optical properties of thin SiO_2 films from 3 to 325 nm in thickness. Using a biased estimator fitting technique, the raw ellipsometric data can be fitted to an air–SiO_2–interface–Si model, where the optical functions of the SiO_2 layer and the interface region are approximated using one-term Sellmeier approximation, and a 50% void, 50% SiO_2 Bruggeman effective medium approximation respectively. The refractive index of the SiO_2 layer is dependent on film thickness, increasing with decreasing film thickness, but always being greater than that of fused quartz. The thickness of the interfacial region increases with increasing film thickness, being less than 0.2 nm for film thicknesses less than 20 nm.

1. Introduction

Ellipsometry is a technique whereby elliptically polarized light is reflected from a sample surface, analyzed with another polarizer, and detected. Historically, ellipsometric data have been used to determine the bulk optical functions of a material or the thickness of an overlying film. Recently, ellipsometric data from more complicated sample surfaces has been interpreted in terms of surface roughness or film composition. Ellipsometry configurations can take many different forms; in all cases, the ellipsometric angles ψ and Δ are determined, where

$$\rho = r_p/r_s = \tan \psi \, e^{i\Delta} \tag{1}$$

The quantities $r_p(r_s)$ are the complex Fresnel reflection coefficients for light polarized parallel (perpendicular) to the plane of incidence. Alternatively, the ellipsometric data can be expressed in terms of the associated ellipsometry parameters:

$$N = \cos 2\psi \tag{2a}$$

$$S = \sin 2\psi \sin \Delta \tag{2b}$$

$$C = \sin 2\psi \cos \Delta \tag{2c}$$

It should be noted that N, S, and C are not strictly independent, since $N^2 + S^2 + C^2 = 1$.

The simplest and most accurate ellipsometers are the nulling ellipsometers (NEs), which operate at a single wavelength, and the ellipsometry angles ψ and Δ are determined by extinguishing the light after the analyzer. These instruments have been commercially available for many years and are well understood [1].

Rotating analyzer ellipsometers (RAEs) are the most popular spectroscopic ellipsometers available today, and are based on a design first described by Aspnes and Studna [2]. In the RAE design, the incident light is plane polarized, and the reflected light passes through the analyzer polarizer which rotates at frequencies in the range 20–100 Hz. The RAE measures $(\cos 2\theta_p - N)/(1 - N \cos 2\theta_p)$ and $(C \sin 2\theta_p)/(1 - N \cos 2\theta_p)$, where θ_p is the azimuthal angle of the polarizer. The calibration and operation of the RAE are well understood, and have become a *de facto* industry standard; commercial RAEs are now available.

However, the RAE suffers from some inherent defects. (1) The time resolution of the ellipsometer is limited to about 0.1 s (owing to the analyzer rotation frequency of 20–100 Hz). (2) Without a phase-retarding optical element, the RAE is limited to measuring quantities proportional to N and C; therefore the RAE is very insensitive to Δ when Δ is near 0° and 180°. (3) The RAE cannot measure the sign of Δ. Problems (2) and (3) can be partially solved by the incorporation of a compensator in the light path or by changing the azimuthal angle of the polarizer, but this solution is not general.

Before the design of the RAE, Jasperson and Schnatterly [3] designed and built an ellipsometer which alleviates many of the shortcomings of the RAE. This ellipsometer uses a photoelastic modulator as the

0040-6090/91/$3.50

compensating element, and is called a polarization modulation ellipsometer (PME), since the light incident upon the sample is dynamically elliptically polarized. This instrument is capable of measuring N, S, or C, but a determination of all three requires at least three scans. Drevillon *et al.* [4] modified the detection circuit, replacing the lock-in amplifiers with fast digitizers; by determining the amplitudes of both the fundamental and the second harmonic, S and either N or C can be determined in a single scan.

In this paper, a new ellipsometer based on the photoelastic modulator is reviewed; details can be found in refs. 5–7. This ellipsometer, called a two-channel polarization modulation ellipsometer (2-C PME), utilizes a Wollaston prism as the analyzing prism, whereby the reflected beam is split into two orthogonally polarized beams. This instrument has the advantage that N, S, and C can be measured simultaneously, allowing measurements to be made on materials previously inaccessible to spectroscopic ellipsometry investigations, such as thin interfaces on insulators [8], intermediate values of the absorption coefficient [5, 8], and enabling the study of thin SiO_2 films on silicon [9].

As an example of the utility of this instrument, the results of an ellipsometric study of thin SiO_2 films on silicon [9] will be reviewed. In general, very thin films of SiO_2 on silicon have not been examined using ellipsometry techniques, since, to first order, the measured parameters are functions of the product of the film thickness and the refractive index. If extremely accurate ellipsometric measurements can be made, then it is possible to see second-order effects, which can decouple the effects of film thickness and refractive index. The 2-C PME is ideal for spectroscopic ellipsometry studies of thin SiO_2 films on silicon, since it alone can make very accurate, spectroscopic measurements of the ellipsometric angle Δ.

2. Description of the two-channel polarization modulation ellipsometer

The 2-C PME ellipsometer that has been set up in our laboratory (shown schematically in Fig. 1) was built on an optical bench for optimum flexibility and stability. The broad-band light source is a 75 W xenon lamp in an elliptical mirror housing, which is focused onto the entrance slit of a 1/4 m single monochromator, with a 1200 lines per mm replica grating. The output light from the monochromator is collected and quasi-collimated by an off-axis parabolic mirror, and two flat mirrors are used to deflect the light beam; the beam divergence at the sample is less than 0.1°.

The light passes through an aperture, a depolarizer, a filter (to limit scattered light or to remove second-order

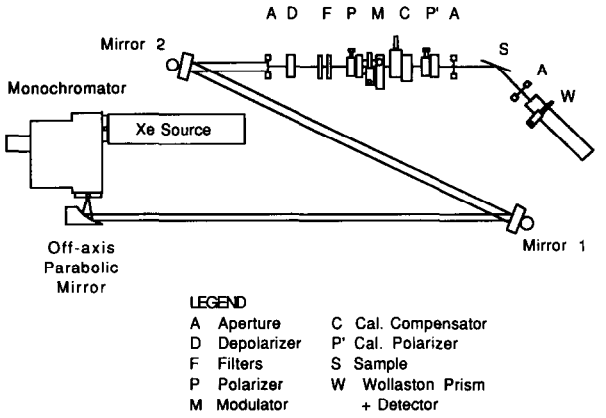

Fig. 1. Schematic diagram of the two-channel polarization modulation ellipsometer.

light), the polarizer–modulator combination (see Fig. 2), and is then incident upon the sample. The reflected light passes through a Wollaston prism, which splits the beam into two mutually orthogonal beams, each of which is detected using a photomultiplier tube (see Fig. 3).

The polarizer–modulator combination consists of a high-quality calcite Glan–Taylor polarizing prism attached directly to the modulator with a manual rotator (0.01° accuracy). Both the polarizer–modulator and the Wollaston-prism–detector combinations are attached to computer-controlled automatic rotators, resulting in 0.02° accuracy in the setting of the respective azimuthal angles.

A schematic diagram of the photoelastic modulator is shown in Fig. 2. An oscillating voltage is applied to a piece of crystalline quartz (c-SiO_2), precisely cut so that an oscillating stress is set up in the i-direction (see Fig. 2). A piece of fused quartz (a-SiO_2) is also precisely cut to resonate at the same frequency, and mechanical coupling to the crystalline quartz sets up a periodic stress in the i-direction of the fused quartz. The frequency of the oscillation is determined by the geometry of the quartz, and is approximately 50.2 kHz in our case. Internal stresses in the fused quartz result in an additional static retardation induced in the modulator.

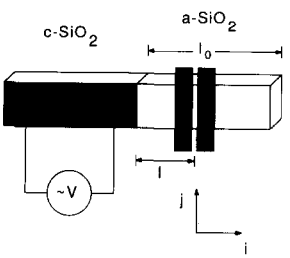

Fig. 2. A schematic diagram of the photoelastic modulator. The a.c. voltage V is applied between the front and back faces of the crystalline quartz component. The black strips represent an aperture which restricts the light to the central part of the fused quartz.

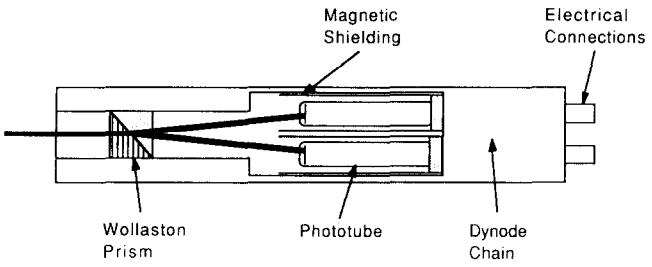

Fig. 3. Wollaston prism and phototube assembly.

The bias voltage of the phototubes shown in Fig. 3 are dynamically controlled such that the d.c. current is constant [7]. The photocurrent from each channel, first converted to a voltage, is measured using a digital voltmeter and two lock-in amplifiers, one tuned to the fundamental frequency and the other tuned to the second harmonic. The entire experiment is computer controlled, and many of the calibration routines are performed automatically. The wavelength range of the instrument is 240–840 nm, determined in the UV by the cut-off of calcite, and in the IR by the phototube response.

3. Theoretical considerations

The intensity of the light reaching the photodetector will have d.c., fundamental, and second harmonic components (as well as higher harmonics), where the fundamental frequency is the resonant frequency of the photoelastic modulator. Generally, the light intensity of the jth harmonic can be expressed as [5]

$$I(j\omega) = a_{j0} + a_{jN}N + a_{jS}S + a_{jC}C \tag{3}$$

where the a parameters are complicated functions of the sines and cosines of the azimuthal angles θ_b (the polarizer with respect to the modulator), θ_m and θ_a (the modulator and analyzer with respect to the plane of incidence at the sample), and of the time-dependent phase retardation introduced by the modulator δ.

The time-dependent retardation introduced by the photoelastic modulator is given by

$$\delta(V_m, \lambda, t) = A(\lambda, V_m)\sin(\omega t) + \delta_0 \tag{4}$$

where V_m is the drive voltage of the modulator, λ is the wavelength of light, $2\pi\omega$ is the frequency of the modulator oscillation, and δ_0 is the retardation of the modulator. Since the phase retardation δ enters the a parameters in eqn (3) as an argument of sines and cosines [5], the intensities of the fundamental and second harmonic will be proportional to the integer Bessel functions $J_1(A)$ and $J_2(A)$ respectively, with the $J_0(A)$ term entering as a perturbation. Generally, V_m is set such that the Bessel angle A is 2.4048 rad (approximately 137.79°), resulting in $J_1(A)$ and $J_2(A)$ being within 15% of their maxima and $J_0(A) = 0$, thus simplifying the data analysis.

Generally, the most useful angles for measurement are $\theta_b = \pm_b 45°$ and $\theta_a = \pm_a 45°$; we will assume these angles throughout the rest of this paper unless otherwise stated. With these restrictions, there are three classes of azimuthal angle orientations which are of interest in PME measurements:

$$(1)\ \theta_m = \pm_m 45° \quad I(\text{d.c.}) \propto 1 \tag{5a}$$

$$I(\omega) \propto \pm_a 2J_1(A)S \tag{5b}$$

$$I(2\omega) \propto \mp_m 2J_2(A)N \tag{5c}$$

$$(2)\ \theta_m = 0°, 90° \quad I(\text{d.c.}) \propto 1 \tag{6a}$$

$$I(\omega) \propto \pm_a 2J_1(A)S \tag{6b}$$

$$I(2\omega) \propto \mp_m \pm_a 2J_2(A)C \tag{6c}$$

$$(3)\ \theta_m = \pm_m 22.5° \quad I(\text{d.c.}) \propto 1 \tag{7a}$$

$$\theta_m = \pm_m 67.5° \quad I(\omega) \propto \pm_a 2J_1(A)S \tag{7b}$$

$$I(2\omega) \propto 2J_2(A)(\zeta C \pm_a \chi N)/\sqrt{2} \tag{7c}$$

In eqns. (5)–(7) and above, the notation $\pm_m$ and $\pm_a$ denotes sign changes due to changes in the modulator and analyzer azimuthal angles respectively. The parameters ζ and χ in eqn. (7c) are ± 1, depending on θ_m. These equations have been developed assuming no errors in any of the azimuthal angles or window effects; the general expressions are given in ref. 5.

Cases 1 and 2 are the conventional configurations [3, 4], where the parameters S and/or N or C can be measured. Case (3) is new, and is discussed in more detail in ref. 5. If the d.c., fundamental, and second harmonic intensities of *both* channels are measured, then it is possible to determine N, S, and C simultaneously.

The 2-C PME has several advantages over the conventional RAE. (1) Since N, S, and C are all measured, there is no ambiguity of the sign of ψ or Δ. (2) There is no value of ψ or Δ to which the 2-C PME is insensitive; RAEs measure $\cos\Delta$, making them very insensitive to Δ when $\Delta \approx 0°$ or 180°. (3) The time response of the PME is approximately 500 times faster than that of an RAE. (4) Since N, S, and C are measured, the sum of the squares can be calculated; this allows for on-line checks of the experiment and a renormalization of N, S, and C (see ref. 5).

4. Example: SiO_2 films on Si

4.1. Introduction

Thin films of SiO_2 grown on silicon have been the subject of many ellipsometry studies over the last few years; in fact, single-wavelength NE is routinely used to

determine the thickness of an insulating film (such as SiO_2) on silicon [1]. Generally, the analysis of ellipsometry data from SiO_2 films on silicon assumes that the optical functions of SiO_2 correspond to those of bulk fused silica and that no interfacial layer exists between the silicon substrate and the SiO_2 thin film.

Several studies [10, 11] of relatively thick SiO_2 layers on silicon have shown that many of these simplifying assumptions used in the interpretation of NE data are not valid. In particular, the interpretation of the ellipsometric data requires the existence of an interface layer between the SiO_2 and the silicon substrate, and a refractive index of the SiO_2 layer greater than that of fused silica. Very thin films of SiO_2 on silicon have generally not been examined using ellipsometry techniques since, to first order, the measured parameters are functions of the product of the film thickness and the film refractive index. If extremely accurate spectroscopic ellipsometry measurements can be made, then second-order effects may be used to decouple the effects of film thickness and refractive index.

4.2. Experiment and data reduction

As an example of the utility of the 2-C PME, the results of an ellipsometry study of SiO_2 on silicon will be reviewed (see ref. 9 for details). For this study, 32 different samples of thin film SiO_2 on crystalline silicon [5 Ω cm, float-zoned, (100)] were prepared in a dry oxygen environment using growth temperatures from 800 °C to 1050 °C; the resulting sample thicknesses ranged from approximately 3 nm to 325 nm.

In order to interpret the measurements, the data were first converted to complex ρ (see eqn. (1)); sample spectra in the ρ representation are shown in Fig. 4. The complex ρ data were then fitted to various models, using an unbiased estimator as a figure of merit [12].

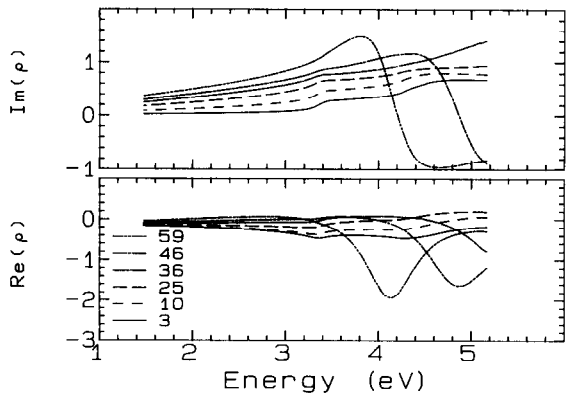

Fig. 4. The real (bottom) and imaginary (top) parts of the complex Fresnel reflection ratio ρ for six thin SiO_2 films on silicon, plotted *vs.* photon energy. The nominal thicknesses of the films are given in nanometers.

The fitting procedure minimizes the χ^2 given by

$$\chi^2 = [1/(n_\lambda - m_z - 1)] \sum_{i=1}^{n_\lambda} [\rho_{\text{calc}}(\lambda_i, z) - \rho_{\text{exp}}(\lambda_i)]^2 / \delta\rho_i(\lambda_i)^2 \tag{8}$$

where the sum goes over the n_λ wavelength points in the spectrum. The calculated spectrum ρ_{calc} is determined from the parameter vector z, which has m_z elements. The elements of the parameter vector z, which may be film thicknesses, constituent fractions, or Sellmeier coefficients, are varied to minimize χ^2. χ^2 is minimized using a Levenberg–Marquardt minimization algorithm, and the variance-covariance matrix and a "goodness of fit" parameter are calculated [11, 12].

As is discussed at length in ref. 12, χ^2 has significant meaning in determining whether the fit is actually consistent with the data only if the errors in the data ($\delta\rho_i$) are included in eqn. (8), and the errors are normally distributed. Under these circumstances, $\chi^2 \approx 1$ indicates that the fit is consistent with the data, while $\chi^2 \gg 1$ indicates that the model does not fit the experimental data.

The models used to fit the data each assume that the ambient was vacuum ($n = 1$) and consist of three media: (1) an SiO_2 film, modeled using a single-term Sellmeier approximation, (2) a thin interfacial layer, modeled using the Bruggeman effective medium approximation [13], assuming a 50% mixture of fused SiO_2 and crystalline silicon, and (3) a crystalline silicon substrate.

The fits to the data were performed by varying some of the following parameters: (1) the thickness of layer 1, d_1; (2) the Sellmeier A coefficient of layer 1; (3) the Sellmeier λ_0 coefficient of layer 1; and (4) the thickness of layer 2, d_2. The optical functions of the SiO_2 layer were determined from a single-term Sellmeier approximation:

$$n^2 - 1 = A\lambda^2/(\lambda^2 - \lambda_0^2) \tag{9}$$

where it was assumed that the film was non-absorptive (*i.e.* $k = 0$). A single-term fit to the data of Malitson [14] between 240 and 780 nm yields $A_{SiO_2} = 1.09905$ and $\lambda_{SiO_2} = 92.27$ nm, with an average absolute residual in the refractive index of approximately 0.0002.

The optical properties (refractive index n and extinction coefficient k) of the silicon substrate were determined from separate 2-C SPME measurements of a (100) sample of crystalline silicon which had been stripped of most of its oxide overlayer. The data were then mathematically corrected for the approximately 7 Å excess oxide remaining after the cleaning, which was modeled using the Sellmeier approximation, with $A = 2.0$ and $\lambda_0 = 92.27$ nm (see below). The thickness of the overlayer was chosen such that the extinction coefficient $k_{Si} = 0.018$ at $\lambda = 630$ nm [15].

The most appropriate fit for the thickest films ($d_1 > 100$ nm) included the variables d_1, A, λ_0, and d_2, holding $f_2 = 0.5$; thinner films ($25\text{ nm} < d_1 \leqslant 100$ nm) were most appropriately fitted using the variables d_1, A, and d_2, holding $\lambda_0 = 92.27$ nm and $f_2 = 0.5$; and the thinnest films ($d_1 \leqslant 25$ nm) were most appropriately fitted using the variables d_1 and A, keeping $\lambda_0 = 92.27$ and eliminating the interface layer [9].

4.3. *Results from the fitting procedure*

Figure 5 shows the values of the Sellmeier A coefficient and selected error limits plotted *vs.* the log of the SiO_2 film thickness. The value of A is greater than the value of A for fused silica (shown by the solid line in Fig. 5) for all samples, and the fitted values of A and their errors increase with decreasing d_1. A linear plot shows that the extrapolated value for A is approximately 2.0 for very thin SiO_2 films on silicon. (Hence the rationale for using $A = 2.0$ in calculating n and k for silicon mentioned above.) This increase in A corresponds directly to an increase in the refractive index with decreasing film thickness. There is, however, no clear dependence of the Sellmeier A coefficient on growth temperature.

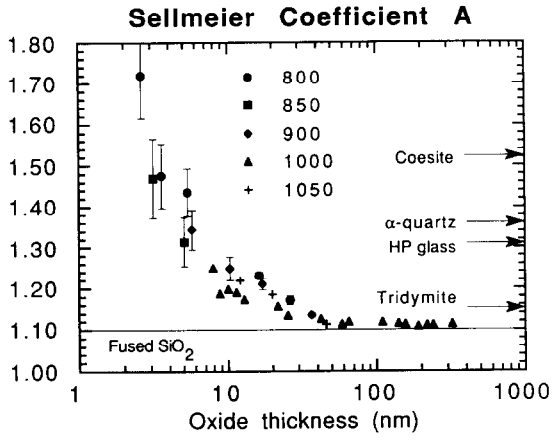

Fig. 5. Sellmeier A coefficient plotted *vs.* the log of the thickness of the SiO_2 layer. The values of A of various high-index polymorphs of crystalline SiO_2 are shown to the right by the arrows. The straight line at $A = 1.099$ corresponds to the A for fused silica. The data sets are labeled by their growth temperatures.

Figure 6 shows a plot of the calculated interfacial layer thickness d_2 from samples with oxide thicknesses greater than 25 nm. Clearly, the interfacial layer thickness increases with increasing film thickness, although there is sizable sample-to-sample variation; there is no discernible dependence of d_2 on growth temperature.

Table 1 presents a list of some of the polymorphs of SiO_2, along with some of their characteristics. The table lists two types of amorphous SiO_2: the normal fused silica, and a high pressure form found by Xie *et al.* [17]. Several crystalline forms are listed, including tridymite and cristobalite, which are metastable and have a relatively low refractive index, and coesite and stishovite, which are stable, but only at high pressures and temperatures. Coesite, which consists of SiO_4 units in four-membered rings, represents the highest packing density (hence the highest refractive index) that can be obtained with SiO_4 units; stishovite consists of SiO_6 units.

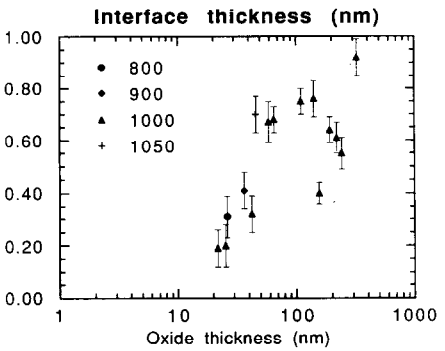

Fig. 6. The interfacial layer thickness plotted *vs.* the log of the SiO_2 thickness for several samples included in this study. The data sets are labeled according to their growth temperatures.

TABLE 1. Various properties of polymorphs of crystalline SiO_2 and fused silica

Material	Density ($g\,cm^{-3}$)	n	A	CN	Reference	Description
fused silica	2.20	1.459	1.099	4	16	normal glass form
α-tridymite	2.26	1.475	1.147	4	16	metastable below 117 °C
α-cristobalite	2.33	1.485	1.176	4	16	Metastable below 267 °C
keatite	2.50	1.519	1.275	4	16	Synthetic, 380–585 °C, 0.33–1.2 GPa
HP-glass	2.56	1.532	1.314	4	17	300 °C, 9.8 GPa
α-quartz	2.65	1.547	1.359	4	16	Stable below 573 °C
coesite	2.92	1.596	1.509	4	16	Stable for >500 °C, >2.0 GPa
stishovite	4.28	1.815	2.238	6	16	Stable for >7.6 GPa

The quantity n is the refractive index at 589 nm and A is the Sellmeier coefficient (see eqn. (5b), assuming $\lambda_0 = 92.27$ nm. CN is the silicon coordination number for each form. Stable temperatures and pressures are listed in the description column.

The Sellmeier A coefficients (at $\lambda = 589$ nm, assuming $\lambda_0 = 92.27$ nm) are shown by the arrows to the right of Fig. 5 for some of the polymorphs.

The Sellmeier A data (or equivalently, the refractive index) presented in Fig. 5 and the data on crystalline materials shown in Table 1 suggest that the structure of thin SiO_2 films consists of amorphous analogs of coesite, quartz, keatite, cristobalite, and tridymite. Since the lattice mismatch between silicon and any form of SiO_2 will result in a very large, compressive stress, it is reasonable that there will be a tendency for denser forms to be created. The thinnest films (2–5 nm) would consist primarily of SiO_4 tetrahedra arranged in four-membered rings, analogous to coesite. Thicker films (5–10 nm) would increasingly add five- or six-membered rings, with relatively close packing (similar to quartz), while even thicker films (greater than 10 nm) would consist of an increasing number of looser packed SiO_4 units, arranged in six-membered rings, reminiscent of cristobalite or tridymite. Even the thickest films do not have as low an A coefficient as fused silica, and so are closer packed than fused silica.

Acknowledgments

This research is sponsored by the Division of Materials Sciences, U.S. Department of Energy under contract DE-AC05-84OR21400 with Martin Marietta Energy Systems, Inc.

The submitted manuscript has been authored by a contractor of the U.S. Government under contract No. DE-AC05-84OR21400. Accordingly, the U.S. Government retains a nonexclusive, royalty-free license to publish or reproduce the published form of this contribution, or allow others to do so, for U.S. Government purposes.

References

1 R. M. A. Azzam and N. M. Bashara, *Ellipsometry and Polarized Light*, North-Holland, Amsterdam, 1977.
2 D. E. Aspnes and A. Studna, *Appl. Opt.*, *14* (1975) 220–228.
3 S. N. Jasperson and S. E. Schnatterly, *Rev. Sci. Instrum.*, *40* (1969) 761–767; *41* (1970) 152.
4 B. Drevillon, J. Perrin, R. Marbot, A. Violet and J. L. Dalby, *Rev. Sci. Instrum.*, *53* (1982) 969–977.
5 G. E. Jellison, Jr., and F. A. Modine, *Appl. Opt.*, *29* (1990) 959.
6 G. E. Jellison, Jr., and F. A. Modine, *SPIE Proc.*, *1166* (1990) 231.
7 G. E. Jellison, Jr., and F. A. Modine, *Rev. Sci. Instrum.*, *60* (1989) 3345.
8 G. E. Jellison, Jr., and B. C. Sales, submitted to *Appl. Opt.*
9 G. E. Jellison, Jr., *J. Appl. Phys.*, *69* (1991) 7627.
10 E. Taft and L. Cordes, *J. Electrochem. Soc.*, *126* (1979) 131–134.
E. A. Taft, *J. Electrochem. Soc.*, *125* (1978) 968–971.
11 D. E. Aspnes and J. B. Theeten, *Phys. Rev. Lett.*, *43* (1979) 1046–1050.
D. E. Aspnes and J. B. Theeten, *J. Electrochem. Soc.*, *127* (1980) 1359–1365.
12 G. E. Jellison, Jr., *Appl. Opt.*, *30* (1991) 3354–3360.
13 D. A. G. Bruggeman, *Ann. Phys. (Leipzig)*, *24* (1935) 636.
14 I. H. Malitson, *J. Opt. Soc. Am.*, *55* (1965) 1205–1209.
15 W. C. Dash and R. Newman, *Phys. Rev.*, *99* (1955) 1151–1155.
16 S. Maj, *Phys. Chem. Minerals*, *10* (1984) 133–136 and references cited therein.
17 H.-S. Xie, H.-G. Xu, W.-S. Peng, Y.-M. Zhang and C.-G. Xue, *Kexue Tongbao*, *32* (1987) 474–477.